Hierarchical particle design to mitigate strength-ductility trade-off in aluminum matrix composites

Qianduo Zhuang[a†], Guodong Zhang[b†], Yihao Luan[a], Sijie Wang[a], Qizhen Ren [a], Jingqi Luan[a], Zhenming Yue[a*], Zan Li[b*]

[a] School of Mechanical, Electrical and Information Engineering, Shandong University at Weihai, Weihai 264209, China

[b]State Key Laboratory of Metal Matrix Composites, Shanghai Jiao Tong University, Shanghai 200240, China

Abstract:

The deformation compatibility between the hard nonmetallic particles and the continuous metal is a challenging issue for the metal matrix composites, mainly due to the bad stress and strain concentrations, and the premature crack around the phase interfaces. The hierarchical size distributions of reinforcing particles have been proved one effective route to reduce the stress concentration around the reinforcement particles. In this work, we focus on the mechanical responses and hardening mechanism analysis of the hybrid SiC particle reinforced aluminum matrix composites with developed microstructural-based strain gradient material model. Hierarchical particle design strategy in 2D representative volume element (RVE) is realized with considering two nonmetallic SiC particle sizes. The effects of particle size, volume fraction and volume ratio of the blend reinforcement on overall numerical mechanical responses are detailed discussed. Different from the traditional monolithic SiC reinforcement, the results show that the hierarchical particle distribution can homogenize deformation and release the stress concentration at the interface, which improve the overall ductility and toughness of composite.

Keyword: Finite element model; aluminum matrix composites; hierarchical particle structure; strength and ductility; stress concentration

1. Introduction

Aluminum alloys are widely used in the automotive and aerospace industries due to their excellent mechanical properties, castability, and corrosion resistance [1-4]. To further enhance the mechanical performance of aluminum alloys, the addition of hard ceramic particles, such as silicon carbide (SiC), alumina (Al_2O_3), and titanium diboride (TiB_2), has been a common method to improve the properties of metal materials [5]. Traditional manufacturing techniques for metal matrix composites include liquid processes, such as casting and liquid infiltration, and solid processes [6], such as powder metallurgy, which have successfully achieved uniform dispersion of reinforcement particles. This is crucial for designing and manufacturing high-performance structural materials. However, during the fabrication of micro-sized

† These authors contributed equally to this work.

* Corresponding authors:
E-mail address: yuezhenming@sdu.edu.cn(Z. Yue), njulizan@sjtu.edu.cn (Z. Li)

silicon carbide particles reinforced aluminum-based (SiC_p/Al) composites, it has been observed that there is a trade-off between strength and toughness, where enhancing/toughening the material sacrifices its toughness/strength. Recent studies have found that nanoscale reinforcements can act as sustainable sources of dislocations under sufficiently high-stress conditions [7, 8], depending on the lattice mismatch between the reinforcements and the matrix. Inspired by this, the introduction of nanoscale reinforcements is considered an effective method to delay crack formation by reducing the local stress concentration of strengthening reinforcements. This redistributes the stress and strain caused by structural heterogeneity, overcoming the challenge of stress concentration in SiC_p/Al composites and thus improving material performance. However, when the composition of the composite changes, it is difficult to predict the mechanical properties and damage behavior of the composite by experiment alone [9, 10].

Microstructure-based numerical simulations have been widely used to predict the macroscopic mechanical properties of multiphase materials [11, 12]. Among various methods, the representative volume element (RVE) model represents macroscopic properties using constitutive characteristics and microstructural features such as volume fraction, size, shape, and distribution [13]. Microstructure-based RVE simulations have been employed to predict the flow behavior, damage evolution, and fracture of various multiphase materials, including metal matrix composites with different reinforcements (i.e., single reinforcement reinforced composites [14-17], and hybrid reinforcements reinforced composites [18, 19]) and composite structures (i.e., the spatial distribution of reinforcing particles) [20]. This approach has also shown promise in simulating the damage evolution at the microscale, aiding in the understanding and prediction of the strength and ductility of SiC_p/Al composites. However, there are still two unresolved issues: (1) the influence of hybrid configurations on mechanical properties has rarely been studied, and (2) numerical studies have only used constitutive equations based on strain gradients or traditional ductile damage, without fully considering the effect of dislocation strengthening on ductility.

In this study, a constitutive model coupling dislocations and damage was established. The two-dimensional (2D) RVE models of SiC_p/Al composites with different particles were subjected to uniaxial tensile mechanical deformation using the user subroutine interface of ABAQUS. To validate the accuracy of the constitutive model, micro-SiC_p/Al composites and hybrid SiC_p/Al composites were prepared, and the numerically simulated stress-strain curves were compared with experimental results of SiC_p/Al composites. The results showed excellent agreement between the simulated stress-strain curves and the corresponding experimental curves. To further investigate the influence of hybrid configurations on mechanical properties, RVE models of SiC_p/Al composites with different particle contents and sizes were constructed using a self-developed Python-based program. The results demonstrated that a small amount of nano-SiC_p could significantly enhance the material performance and predict the ultimate tensile strength and ductility levels of the hybrid configurations.

2. Details of modelling

2.1 Constitutive equations

For an elastoplastic solid, the strain rate $\dot{\varepsilon}_{ij}$ can be decomposed into elastic and plastic parts

$$\dot{\varepsilon}_{ij} = \dot{\varepsilon}^e_{ij} + \dot{\varepsilon}^p_{ij} \quad (1)$$

Based on Hooke's law, the elastic part $\dot{\varepsilon}^p_{ij}$ can be derived from the stress rate $\dot{\sigma}_{ij}$

$$\dot{\varepsilon}^e_{ij} = \frac{1}{2\mu}\dot{\sigma}'_{ij} + \frac{\dot{\sigma}_{kk}}{9k}\delta_{ij} \quad (2)$$

where μ and K are shear and bulk moduli, respectively. $\dot{\sigma}'_{ij} = \dot{\sigma}_{ij} - \frac{1}{3}\dot{\sigma}_{kk}\delta_{ij}$ is the deviatoric stress rate. Based on the J2-flow theory of plasticity, the plastic strain rate $\dot{\varepsilon}^p_{ij}$ can be derived from the deviatoric stress σ'_{ij},

$$\dot{\varepsilon}^p_{ij} = \frac{3\dot{\varepsilon}^p}{2\sigma_e}\sigma'_{ij} \quad (3)$$

where $\sigma'_{ij} = \sigma_{ij} - \frac{1}{3}\sigma_{kk}\delta_{ij}$, and $\sigma_e = \sqrt{\frac{2}{3}\sigma'_{ij}\sigma'_{ij}}$ is the the von Mises effective stress. $\dot{\varepsilon}^p = \sqrt{\frac{3}{2}\dot{\varepsilon}^p_{ij}\dot{\varepsilon}^p}$ is the equivalent plastic strain rate. Based on the power law visco-plastic formulation [21], $\dot{\varepsilon}^p$ can be derived from σ_e.

$$\dot{\varepsilon}^p = \dot{\varepsilon}\left(\frac{\sigma_e}{\sigma_f}\right)^m \quad (4)$$

where $\dot{\varepsilon} = \sqrt{2\dot{\varepsilon}'_{ij}\dot{\varepsilon}'_{ij}/3}$ is the effective strain rate, and $\dot{\varepsilon}'_{ij} = \dot{\varepsilon}_{ij} - \dot{\varepsilon}_{kk}\delta_{ij}/3$ denotes the deviatoric strain rate. m is the rate sensitivity exponent.

2.2 Deformation mechanism

The metal matrix in the composite is modeled as an isotropic elasto-plastic material and its strain hardening is controlled by the dislocation density. Metal matrix in composites produces gradient strain distributions due to uncoordinated deformation. The plastic strain gradient needs to be accommodated by the polarized distribution of geometrically necessary dislocations (GNDs) [22]. Statistically stored dislocations (SSDs) and GNDs contribute to isotropic hardening, and the contribution of dislocations to the flow stress is known as σ_{Taylor} [23, 24]. The flow stress is expressed as

$$\sigma_f = \sigma_0 + \sigma_{HP} + \sigma_{Taylor} \quad (5)$$

σ_0 is the lattice friction stress. $\sigma_{HP} = k_{hp}/(d)^{1/2}$ represents the grain boundary strengthening, where k_{HP} is the Hall-Petch slop and d is grain size [25]. $\sigma_{Taylor} = M\alpha\mu b\left(\rho_{SSDs} + \rho^{sam}_{GNDs} + \rho^{gra}_{GNDs}\right)^{1/2}$ is the Taylor flow stress

term [22], where M, α, μ, b, ρ_{SSDs}, ρ_{GNDs}^{sam} and ρ_{GNDs}^{gra} are the Taylor factor, the Taylor constant, the magnitude of Burgers vector, the density of SSDs, sample level GNDs, and grain level GNDs, respectively.

The evolution of ρ_{SSDs} with the equivalent plastice strain ε^p is expressed as [26-28]

$$\frac{\partial \rho_{SSD}}{\partial \varepsilon^p} = M\left(\frac{k_1}{bd}+\frac{k_2}{b}\sqrt{\rho_{SSD}+\rho_{GND}}-k_3\left(\frac{\dot{\varepsilon}^p}{\dot{\varepsilon}_{ref}}\right)^{-\frac{1}{n_0}}-\left(\frac{d_{ref}}{d}\right)^2\rho_{SSD}\right) \quad (6)$$

On the right side of the equation, the first term accounts for the contribution of grain boundary enhanced dislocation storage, which is influenced by the geometrical parameter k_1 related to the shape of the grain. The second term represents the dislocation multiplication dependent on the free slip path, incorporating the effect of GNDs. The proportionality factor k_2 determines the strength of this effect. The third term considers the dynamic recovery, which is assumed to be independent of GNDs [26, 29] and is characterized by the dynamic recovery exponents k_3 and n_0. The reference strain rate ε_{ref} is used to scale the dynamic recovery term. The last term describes the additional annihilation effect due to the presence of grain boundaries, where d_{ref} represents the reference grain size [30, 31].

At the sample level, GNDs may be distributed across different phases. By the effective plastic strain gradient, the GND density is expressed as [23, 32]

$$\rho_{GNDs}^{sam} = \bar{r}\frac{\eta^p}{b} \quad (7)$$

where $\bar{r}$ is the Nye factor [33]. η_p is expressed as $\eta^p = \sqrt{\frac{1}{4}\eta_{ijk}^p\eta_{ijk}^p}$, where $\eta_{ijk}^p = \varepsilon_{ik,j}^p + \varepsilon_{jk,i}^p - \varepsilon_{ij,k}^p$ [34]. In the FEM simulation, the macroscopic strain gradient is realized by the gradient of the shape function.

Grain level GNDs distributed between grain boundaries is expressed as

$$\rho_{GNDs}^{gra} = \frac{N}{d^2} \quad (8)$$

where d and N are the grain size and the total number of piled-up dislocations, respectively. The evolution of N with plastic strain is expressed as [35]

$$\partial N / \partial \varepsilon^P = N_\Delta\left(1 - N / N^*\right) \quad (9)$$

where N^* is the saturation number of dislocations in grain boundaries, and $N_\triangle$ is the initial evolution rate of pileup dislocation. Both N^* and $N_\triangle$ are linearly related to d, i.e.,

$$N^* = \lambda d + N_{extra} \quad (10)$$

$$N_\Delta = k_N d + N_A \quad (11)$$

where λ and N_{extra} are the proportional coefficient and the constant, respectively. k_N is also the pileup dislocation constant.

2.3 Coupled damage model

The coupled damage model can be derived from the continuous isotropic damage variable [36]

$$D = (S_0 - S) / S_0 \quad (12)$$

where S_0 and S are the initial area and the actual area, respectively. When $D=1$, it means that the material is completely damaged. When the damage variable D is coupled with elastic-plastic deformation, Taylor hardening, and isotropic hardening, the following equations can be obtained

$$\underline{\tilde{\varepsilon}} = g_e \varepsilon^e; \quad \underline{\tilde{\sigma}} = \frac{\sigma}{g_e} \quad (13)$$

$$g_e = \sqrt{1-D} \quad (16)$$

The evolution equations of the coupled damage constitutive model are expressed as

$$\dot{D} = \frac{\dot{\lambda}}{(1-D)^{\beta}} \left(\frac{< Y - Y_0 >}{S}\right)^s \quad (17)$$

where $\underline{1}$ represents the unit tensor, and $< >$ represents Macaulay brackets. a and b are the nonlinear parameters of kinematic and isotropic hardenings, respectively. S, s, β, and Y_0 are the parameters governing the evolution of ductile damage. For more details, please refer to the relevant literature [37]. The constitutive model above can be implemented by Fortran programming language through the user subroutine interface UEL in Abaqus software, and used in the subsequent simulations.

In this study, the material properties of the matrix and reinforcement were selected from our previously prepared SiC_p/Al metal matrix composite.

Table. 1 Constitutive parameters of 2024 Al

Parameters	Symbol	Value
Taylor factor	M	3.06
Elasticity modulus (MPa)	E	85704
Poissons ratio	v	0.33
Taylor constant	α	0.26
Burgers vetor (μm)	b	0.000256
Rate sensitivity exponent	m	20
Lattice friction stress (MPa)	σ_0	260
Hall-Petch slop (MPa·μm$^{1/2}$)	k_{HP}	45
Grain size (um)	d	8
Geometric factor	k_1	0.06
Proportionality factor	k_2	0.008
Dynamic recovery factor	k_3	1.5
Dynamic recovery exponent	n_o	21.25
Reference strain rate (S^{-1})	ε_0	1
Reference grain size (μm)	d_{ref}	2

Nye-factor	$\bar{r}$	1.9
Pileup dislocations constant 1 (μm^{-1})	k_N	46
Pileup dislocations constant 2	N_A	300
Pileup factor related to grain size (μm^{-1})	λ	5.9
Effective radius of GNDs domain (μm)	R	3
Correction parameter of pileup dislocations	N_{extra}	0.68
Initial dislocation density (mm^{-2})	ρ_0	2×10^{11}
Damage parameter 1	S	5.0
Damage parameter 2	s	6.0
Damage parameter 3	β	3.0
Damage parameter 4	Y_0	6.0

3. Result

3.1 Effect of nano-particles

In this work, SiC_p/Al composites with different particle sizes and volume fractions were studied. Due to the complexity of the problem and computational cost, the 2D RVE model was chosen instead of the 3D model. The RVEs were subjected to uniaxial tensile deformation to evaluate their mechanical properties. To investigate the ductility of the material, the generation of incomplete particles near the edges of RVEs was prohibited to avoid premature damage initiation (as shown in fig. 1). Considering the balance between computational accuracy and cost, the size of each RVE was set to 50×50 μm^2. The seed spacing for generating the mesh was set to 0.1 μm. Therefore, the total number of elements in each RVE was 250,000. Quadrilateral elements (CPE8 in Abaqus) were used for the shape functions of the mesh.

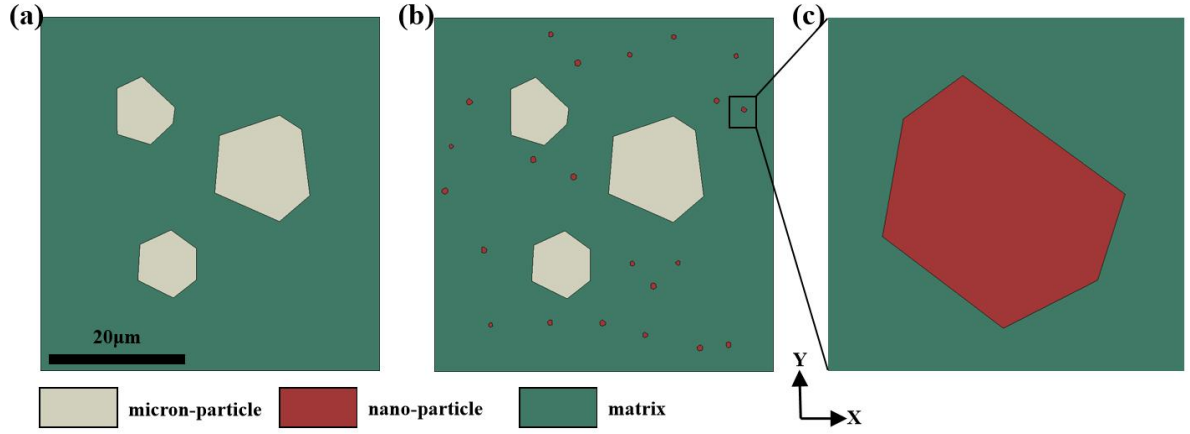

Fig. 1. FEM model (representative volume element) of (a) SiC_{mp}/Al composites and (b) hybrid SiC_p/Al composites. The content of SiC_{np} is 10% and the content of nano-particles is 0.5%. (c) Enlarger view of the SiC_{np} in the (b). Boundary conditions were applied to the edges of these RVE models with the left edge fixed and the right edge moved only in the horizontal (X-axis) direction until fracture occurred.

When only micro-SiC_p (SiC_{mp}) is present, there is a significant difference in the equivalent strain between the particles and the matrix. This difference in the equivalent strain leads to the stress concentration at tips of particles, which can result in the premature damage initiation in the matrix and ultimately lead to the material failure. The figure 2(a) shows the distribution of equivalent strain and Equ stress in RVEs with and without nano-SiC_p (SiC_{np}). Introducing SiC_{np} helps to alleviate the stress concentration at tips of particles by regulating the strain in the matrix. Comparing the stress distribution at tips of particles (fig. 2(c)), it can be observed that the stress in the material with only SiC_{mp} rapidly decreases as the distance from the particle increases. In contrast, the stress in the material with SiC_{np} decreases more slowly as the distance from the SiC_p increases. This trend becomes more pronounced as the engineering strain increases (the difference in stress at particle tips gradually increases, while the difference in stress in the matrix gradually decreases). This is because the nano-particles improve the strain distribution in the matrix and bear more stress (as shown in fig. 3(c)). As the engineering strain increases, the ability of the SiC_{np} to improve the strain distribution in the matrix becomes enhanced (as shown in the fig. 3(a)).

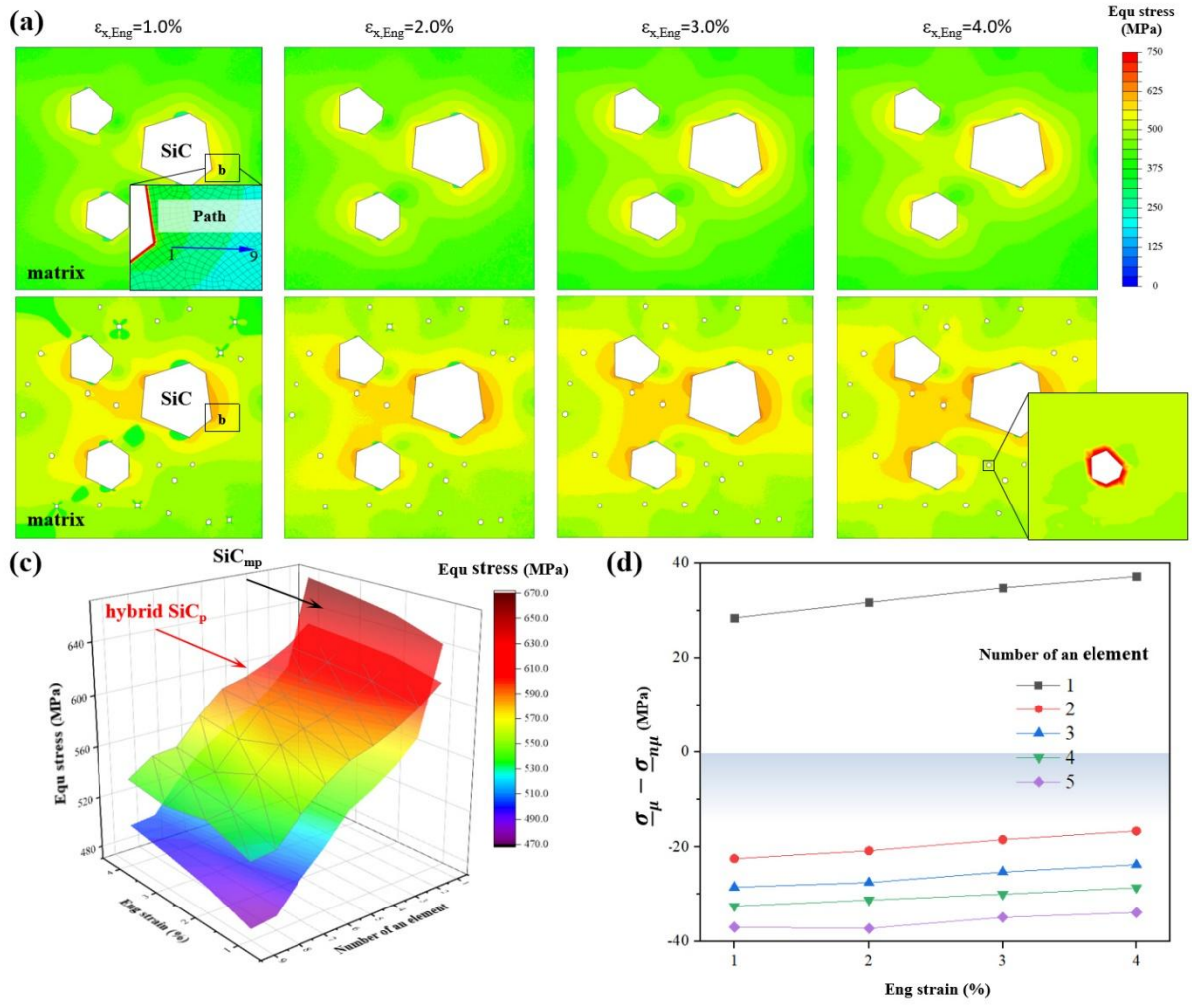

Fig. 2. Analyzed micromechanics at the SiC_p-matrix boundary. (a) An illustration for the partition of engineering strain. The distribution and evolution of Eq stress in cases. (b) Enlarged view of the numbering of an element (for Eq stress extraction) in the (a). (c) Eq stress varies with engineering strain and element numbering. (d) $\underline{\sigma}_{\mu} - \underline{\sigma}_{n\mu}$ varies with engineering strain and element numbering ($\underline{\sigma}_{\mu}$ and $\underline{\sigma}_{n\mu}$ are Eq stress in SiC_{mp}/Al composites and Equ stress in hybrid SiC_p/Al composites, respectively.).

From the macroscopic perspective, hybrid SiC_p/Al composites exhibit higher strength. During plastic deformation, the metal matrix undergoes deformation first, while the reinforcing particles undergo minimal deformation, resulting in localized stress concentration near the reinforcing particles. With more stress "islands" generated around the SiC_{np}, the applied tensile stress is dispersed to the SiC_{np} and its surrounding influence area, leading to improved performance.

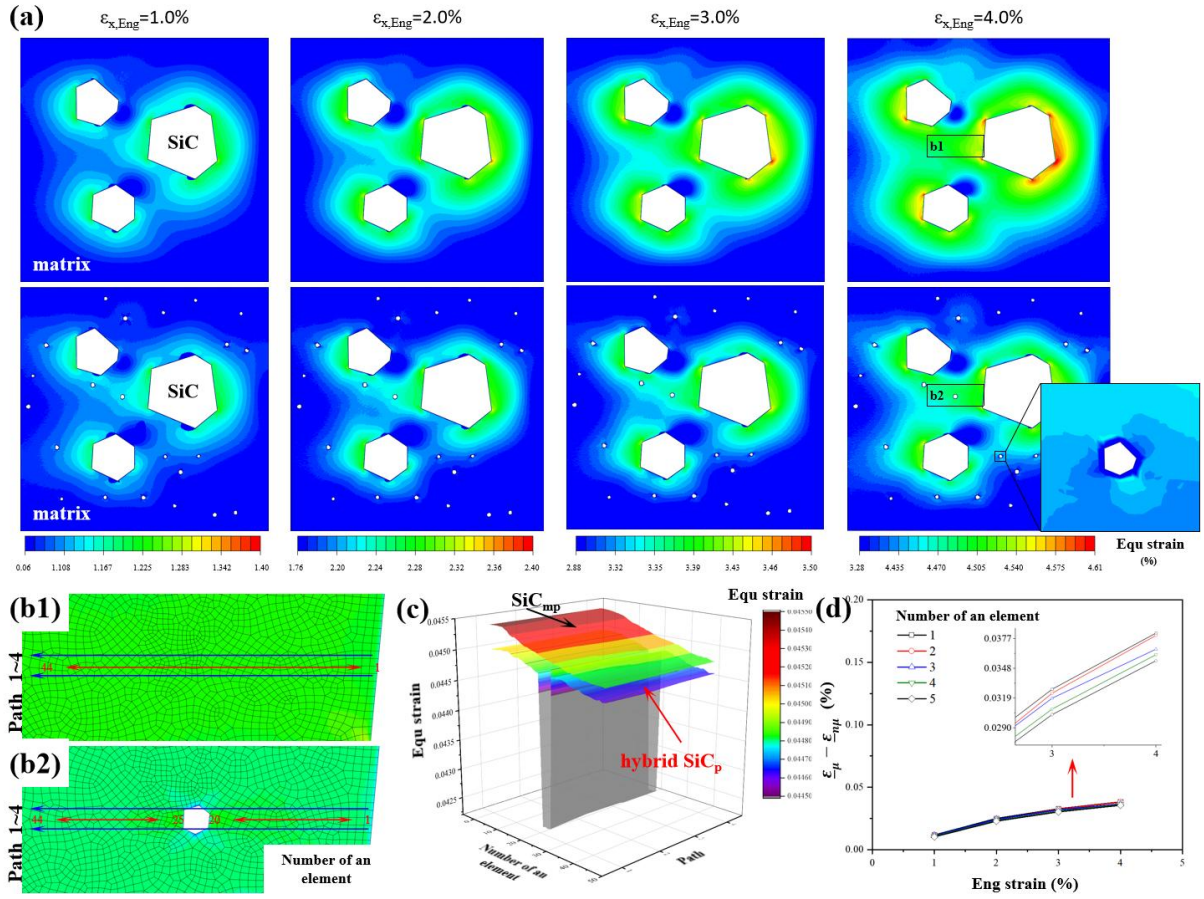

Fig. 3. Analyzed micromechanics at the SiC_p-matrix boundary. (a) An illustration for the partition of engineering strain. The distribution and evolution of equivalent strain in cases. Enlarged view of path and the numbering of an element (for equivalent strain extraction) in the (a): (b1) micron-particle and (b2) micron-/nano-particle reinforced aluminum matrix composites. (c) Equivalent strain varies with path and element numbering. (d) $\underline{\varepsilon}_{\mu} - \underline{\varepsilon}_{n\mu}$ varies with engineering strain and element numbering($\underline{\varepsilon}_{\mu}$ and $\underline{\varepsilon}_{n\mu}$ are Equ strain in SiC_{mp}/Al composites and Equ strain in hybrid SiC_p/Al composites, respectively.).

3.2 Distribution of GNDs

To further investigate the underlying reasons for the improvement in material performance due to the addition of SiC_{np}, the distribution of GNDs was compared. It is easily observed that the density of GNDs around the particles is much higher than that in the bulk (fig. 4(a)). By extracting the dislocations at tips of particles, it can be concluded that it is these factors that contribute to the delay in the initiation of damage in the presence of SiC_{np}.

From a microscopic perspective, SiC_{mp} tends to pin dislocations, while SiC_{np} effectively promotes dislocation multiplication, delocalization, or the formation of dislocation tangles. The movement of dislocations towards the SiC_{mp} is hindered and pinned by the nano-particles. This is how SiC_{np} enhances the matrix without compromising the ductility of the composite material.

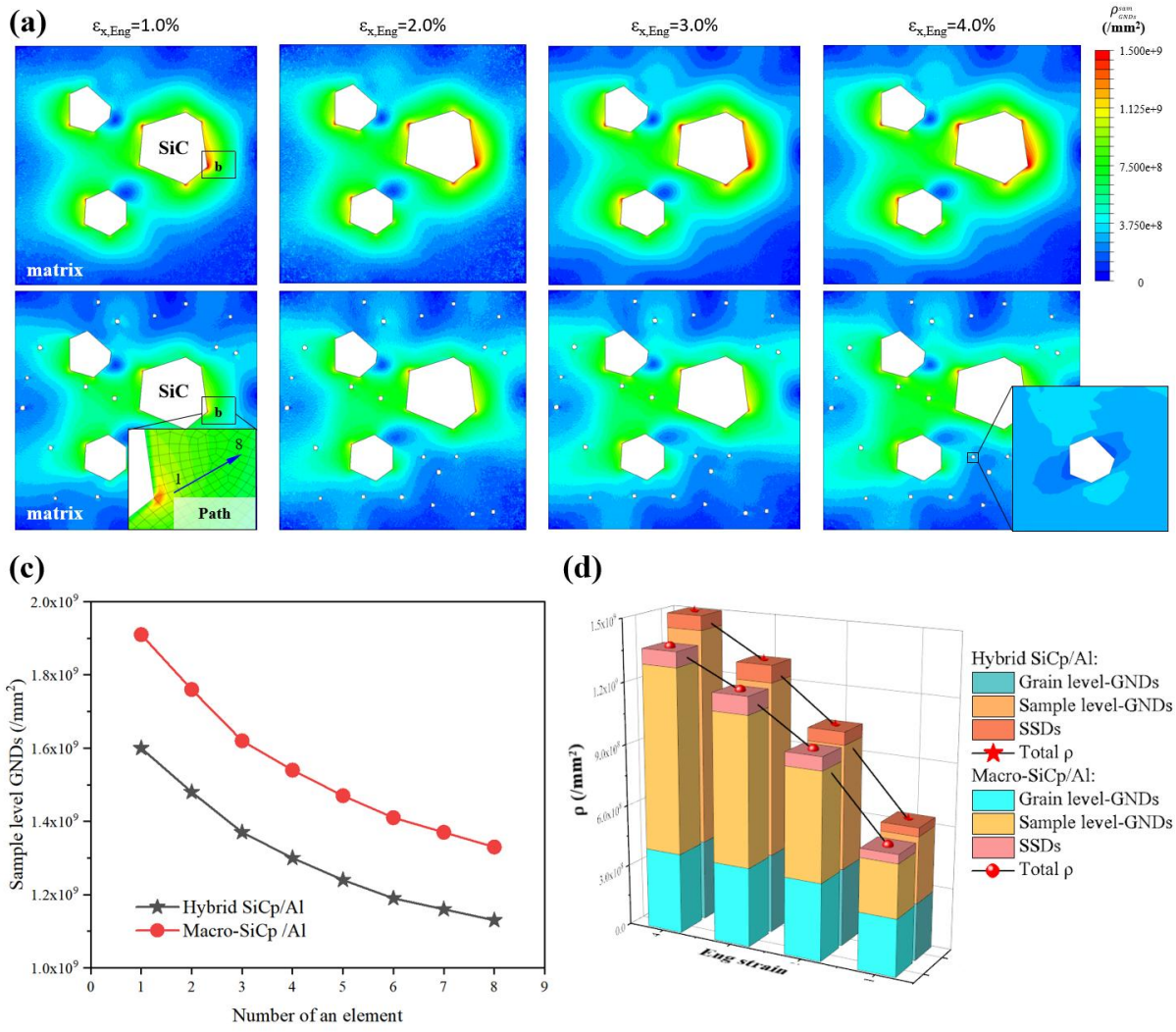

Fig. 4. Analyzed micromechanics at the SiC_p-matrix boundary. (a) An illustration for the partition of engineering strain. The distribution and evolution of ρ_{GNDs}^{sam} in cases. Enlarged view of path and the numbering of an element (for equivalent strain extraction) in the (a). (b) Enlarged view of the numbering of an element in the (a). (c) ρ_{GNDs}^{sam} varies with path and element numbering. (d) The average of

$\tilde{\rho}_{GNDs}^{sam} - \rho_{GNDs}^{sam}$ varies with engineering strain and element numbering.

3.3 Experimental validation

To validate the findings, the stress-strain curves of the experimentally prepared materials were compared with the numerical simulation results of the 2024 Al matrix, SiC_{mp}/Al composites, and hybrid SiC_p/Al composites, as shown in Fig. 5(a). The results demonstrate a close agreement between the simulated stress-strain curves and the corresponding experimental curves, accurately predicting the strength levels in the plastic stage and the ductility in the damage stage. Through Fig. 5(b), it can be observed that the SiC_{mp} and SiC_{np} are evenly dispersed in the matrix. The RVEs above use polygonal SiC particles, which accords with the experimental observation.

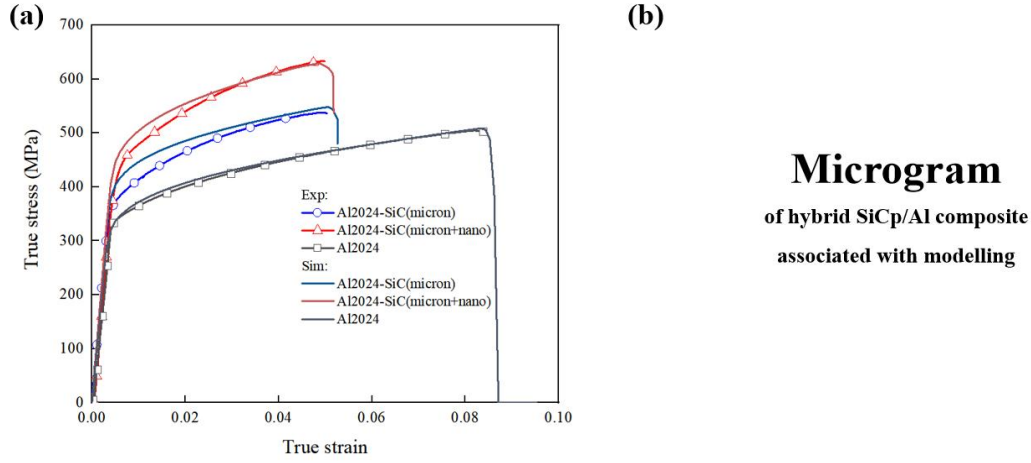

Fig. 5. (a) SiC_p/Al composites compared the model predictions (lines) with experimental measurements (point-lines), which verified the validity of the current plasticity model and the adopted constitutive parameters. (b) Microstructure of hybrid SiC_p/Al composites.

4. Discussion

To further investigate the influence of configuration evolution on the strength and ductility of hybrid SiCp/Al metal matrix composites, additional studies were conducted by varying the total volume fraction of SiC_p, the radius of SiC_{mp}, the radius of SiC_{np}, and the ratio of volume fractions between SiC_{mp} and SiC_{np}, respectively. The configuration parameters are shown in Table 2.

Table. 2 Modeling parameters of RVE

	Num.	SiC_{mp} radius (μm)	SiC_{np} radius (nm)	SiC_{mp} volume fraction (vol.%)	SiC_{np} volume fraction (vol.%)
	1	2.5	200	3.48	0.52
	2	2.5	200	6.96	1.04
4.1	3	2.5	200	10.44	1.56
	4	2.5	200	13.92	2.08
	5	2.5	200	17.40	2.60

4.2	1	3	200	9.13	1.37
	2	4	200	9.13	1.37
	3	5	200	9.13	1.37
	4	6	200	9.13	1.37
	5	7	200	9.13	1.37
	6	9.9	200	9.13	1.37
4.3	1	2.5	200	9.13	1.37
	2	2.5	300	9.13	1.37
	3	2.5	400	9.13	1.37
	4	2.5	500	9.13	1.37
	5	2.5	600	9.13	1.37
	6	2.5	700	9.13	1.37
4.4	1	2.5	200	10.39	0.11
	2	2.5	200	9.76	0.74
	3	2.5	200	9.14	1.36
	4	2.5	200	8.51	1.99

4.1 The effect of particles content

The degree of incompatibility between the constituent phases is a key factor influencing the density of GNDs, which in turn affects the material's performance. Taking the variation in total particle content as an example, the SiC_p content was varied within the range of 4-20 vol.%.

The mismatch in deformation between the SiC_p and the metal matrix leads to incompatibility in the plastic deformation of the metal matrix around particles. The fig. 6(a) shows the distribution of GNDs in the matrix. During the tensile process, higher SiC_p content clearly results in higher GND density in the matrix. As shown in fig. 6(b), the variation trend of ultimate tensile strength (UTS) is the same as the variation trend of average ρ_{GNDs}^{sam}, while the variation trend of ductility is opposite to the variation trend of max ρ_{GNDs}^{sam}. As the total SiC_p content increases, the ultimate tensile strength of the material also increases, but the ductility decreases. This is consistent with the previous rule of strength-ductility trade-off. The higher GND density leads to significant stress differences between the SiC_p and the matrix, which in turn leads to premature damage initiation in the material. Taking the product of UTS and ductility (E_U) as the indicator of strength-toughness combination, and plotting it as a function of the volume fractions of SiC_p (as shown in fig. 6(c)). The optimal strength-toughness combination (with maximum $\sigma_U \times E_U$) can be obtained from versus.

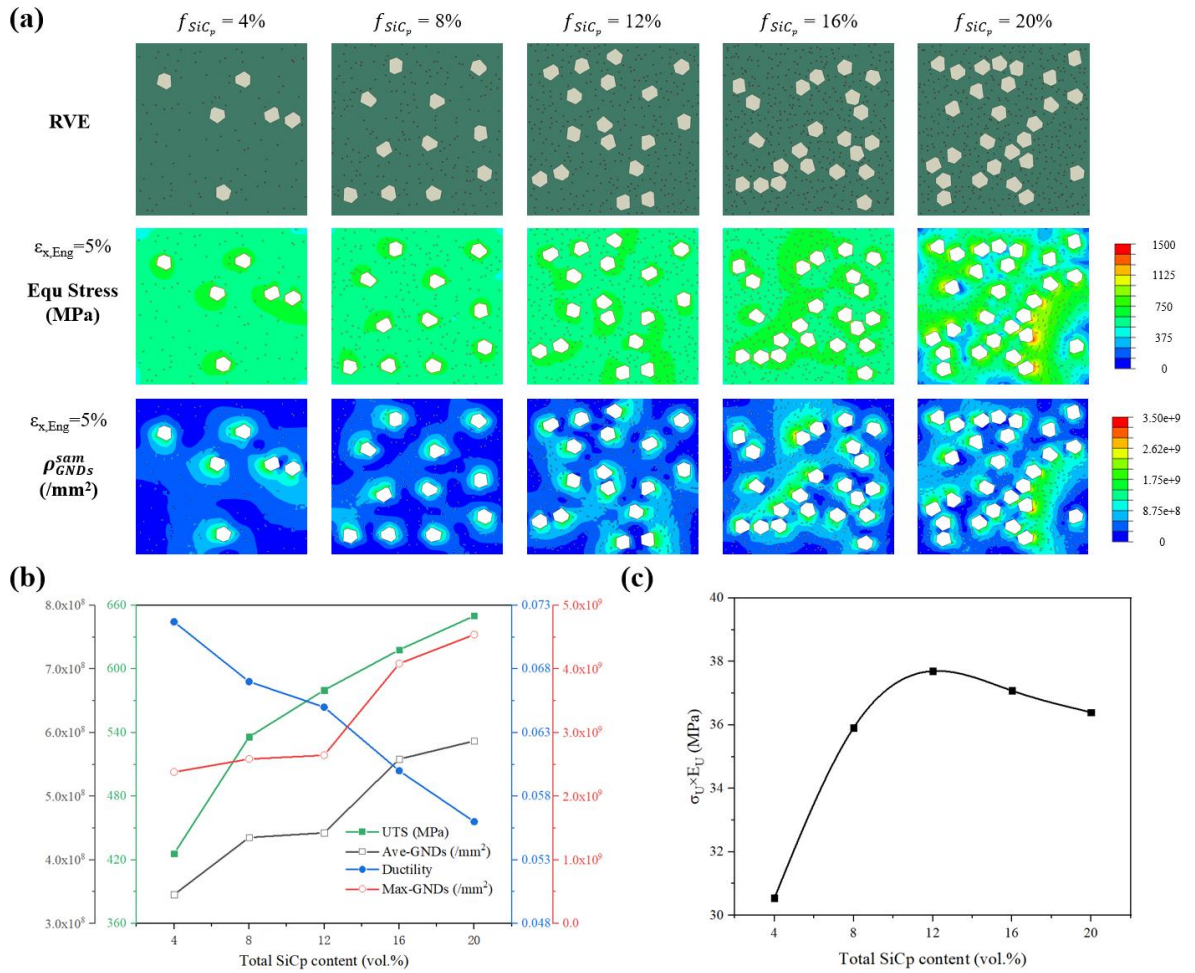

Fig. 6. The influence of volume fractions of particles on SiC_p/Al composites: (a) Equ stress and ρ_{GNDs}^{sam} maps (f_{SiC_p} is the volume fractions of SiC_p), (b) Strength-toughness, average ρ_{GNDs}^{sam}, and max- ρ_{GNDs}^{sam}, (c) $\sigma_U \times E_U$ versus. (σ_U is ultimate tensile strength. E_U is ductility.)

4.2 The effect of macro-particles size

In order to explore the physical origins behind the dependence of different scale heterogeneities on the synergistic mechanical response, a micro-mechanical analysis was conducted based on the influence of SiC_{mp} and SiC_{np} sizes on the density of GNDs.

As the size of SiC_{mp} increases, the density of GNDs around the particles gradually increases, leading to an enhancement in material strength, but accompanied by premature damage initiation (as shown in fig. 7(a)). Before the occurrence of damage, larger SiC_{mp} can induce more severe heterogenous deformation, resulting in a higher density of GNDs (as shown in fig. 7(b)). However, when damage occurs prematurely, the improvement in material strength due to dislocations may not be fully realized, leading to a decreasing trend in the ultimate tensile strength of the material. As shown in the fig. 7(c), the structure with the SiC_{mp} size of 4 μm exhibits a more coordinated stress distribution, seemingly demonstrating the optimal balance between strength and ductility with the higher work hardening.

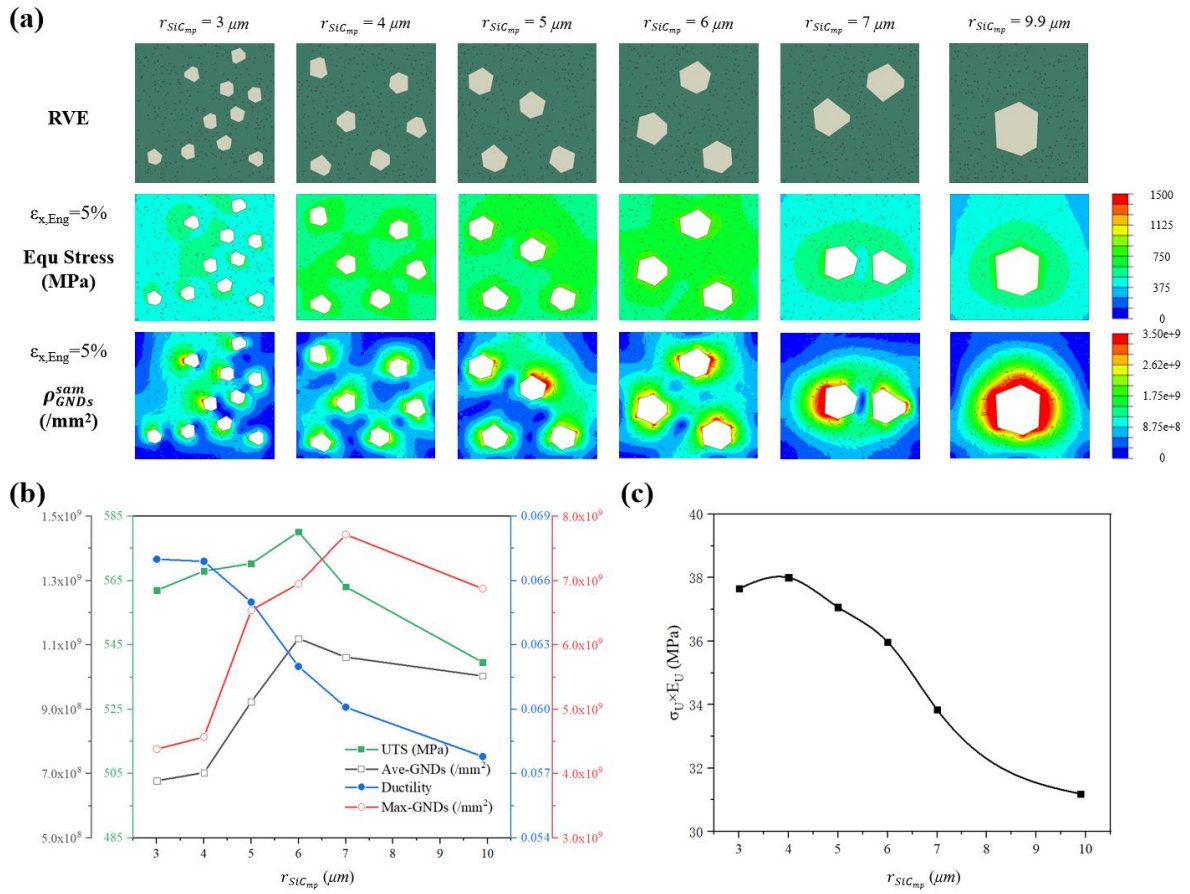

Fig. 7. The influence of sizes of SiC_{mp} on 10.5 vol.% SiC_p/Al composites : (a) Equ stress and ρ^{sam}_{GNDs} maps ($r_{SiC_{mp}}$ is the radius of SiC_{mp}), (b) Strength-toughness, Average ρ^{sam}_{GNDs}, and max ρ^{sam}_{GNDs}, (c) $\sigma_U \times E_U$ versus.

4.3 The effect of nano-particles size

As the size of SiC_{np} increases, the effect on the mechanical response exhibits a different trend. With the increase in the SiC_{np} size, there is a tendency for the occurrence of dislocations to first decrease and then increase. As shown in the fig. 8(b), average ρ^{sam}_{GNDs} was extracted. By comparison, it was found that when the size of the SiC_{np} is very small, regardless of the variation in SiC_{np} size, dislocations caused by heterogenous deformation around the SiC_{np} are almost the same (as shown in fig. 8(a)). This results in a decrease in the total dislocation density as the SiC_{np} size increases due to the reduction in the number of SiC_{np}. However, the stress relief effect at the tip of the SiC_{mp} remains the same.

At a small size of SiC_{np}, the SiC_{np} mainly acts as reinforcement of the matrix and increases the strength of the composite material. However, when the size of the SiC_{np} gradually exceeds a critical value, the trend of dislocations caused by heterogenous deformation becomes similar to the initial variation in SiC_{mp} size (as shown in fig. 7(c) and fig. 8(c)). SiC_p within this size range should be considered as 'submicro-SiC_p'.

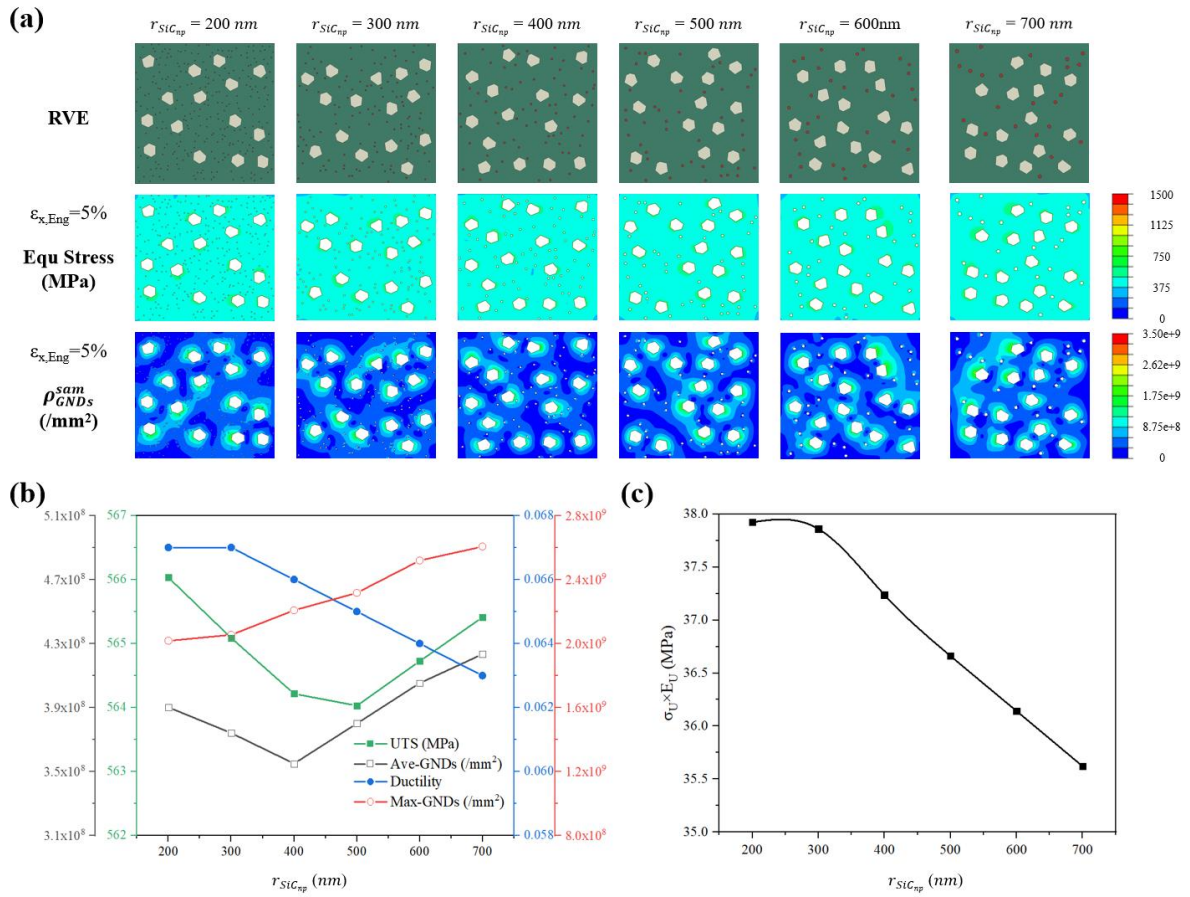

Fig. 8. The influence of sizes of SiC_{np} on 10.5 vol.% SiC_p/Al composites: (a) The maps of Equ Stress and ρ^{sam}_{GNDs} in relation to the variation in $r_{SiC_{np}}$; (b) Investigate the relationship between Strength and Average ρ^{sam}_{GNDs} and the relationship between Toughness and Max- ρ^{sam}_{GNDs}; (c) Analyze the variation of $\sigma_{U\times}E_U$ with changing $r_{SiC_{np}}$.

4.4 The effect of volume ratio of nano-particles to micro-particles

In this study, hybrid SiC_p/Al composites with different parameters were investigated. If the total content of the reinforcing phase remains constant and only the ratio of SiC_{mp} to SiC_{np} is changed, it will provide a clearer understanding of the roles of SiC_{mp} and SiC_{np} in the composite material. As shown in Fig. 9(a), increasing the proportion of SiC_{np} in the particle content leads the strength to first decrease and then increase and an increase in ductility of the material. This further confirms the stress-relieving effect of SiC_{np} in SiC_p/Al composites.

The addition of an appropriate amount of SiC_{np} improves the deformation incompatibility of the matrix and generates stronger interfacial interactions, resulting in a higher strain gradient within the matrix (as shown in Fig. 9(b)). The development of a higher density gradient of the GND field throughout the matrix is expected to alleviate stress concentration. In summary, for engineering heterogeneous structures, off-domain heterogenous deformation contributes to the synergistic enhancement of strength and ductility.

Fig. 9(c) presents that increasing the volume fraction ratio of SiC_{np} to total-SiC_p can simultaneously enhance the strength-toughness combination. However, the effect of improving strength-toughness gradually diminishes as the ratio increases.

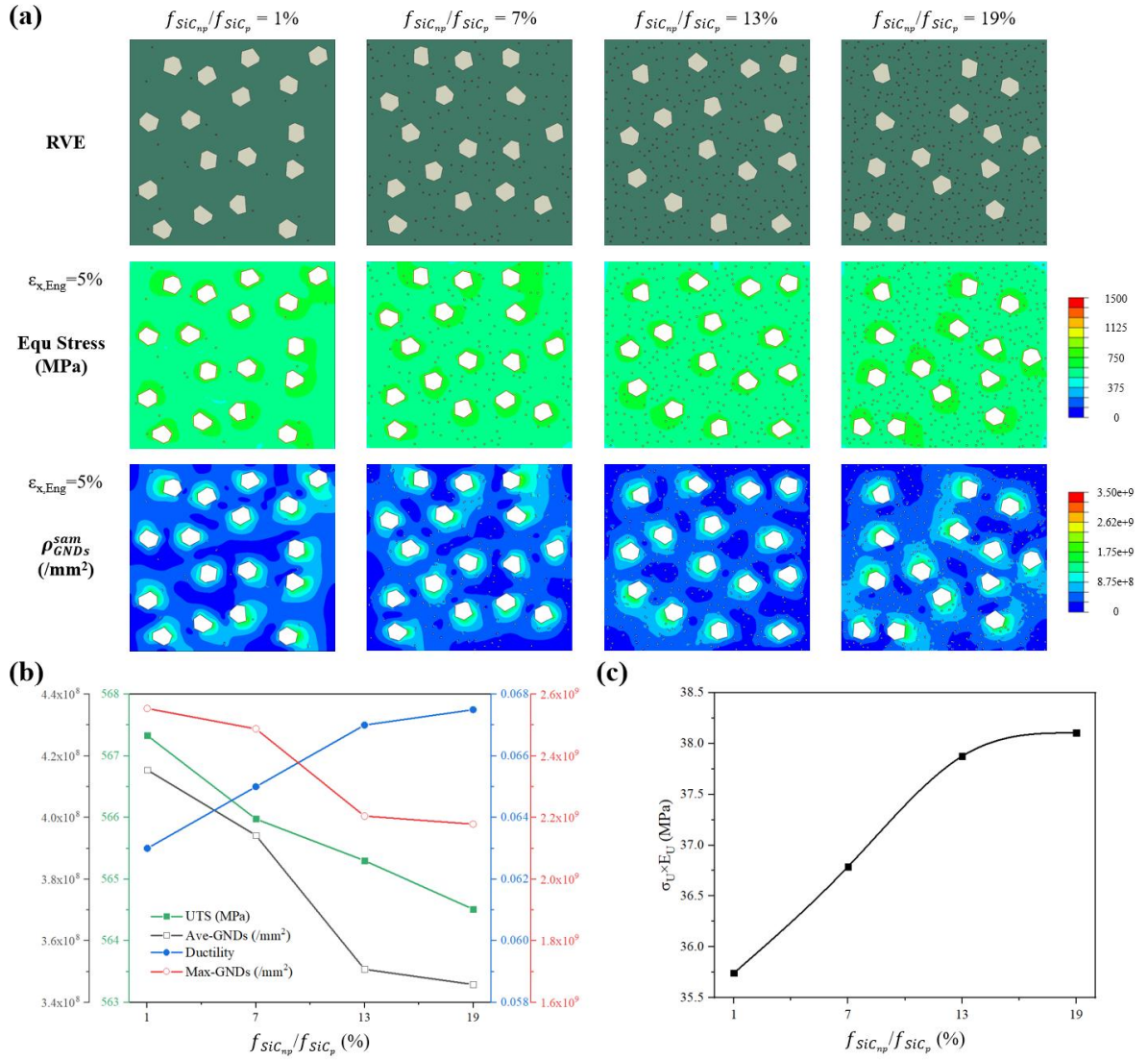

Fig. 9. Investigate the impact of the rate of SiC_{np} to total-SiC_p on 10.5 vol.% SiCp/Al Composites:(a) The maps of Equ Stress and ρ^{sam}_{GNDs} in relation to the volume fraction of SiC_{np} ($f_{SiC_{np}}$); (b) Analyze the relationship between Strength and Average ρ^{sam}_{GNDs} and the relationship between Toughness and Max-ρ^{sam}_{GNDs} ; (c) Examine the Variation of $\sigma_U \times E_U$ with respect to $f_{SiC_{np}}$.

5. Conclusion

In this work, the tensile loading behaviors of metal matrix composites reinforced with hybrid particles having four different conformational parameters are simulated to investigate the effect of nanoscale particles on the mechanical response. With the help of the developed rve geometry means, the two scales of reinforcement phases can be accurately tuned, and in combination with periodic boundary conditions,

the effect of the two scales of reinforcement phases on the overall mechanical properties of the composite is analysed (modulus, yield, tensile strength, elongation). The following conclusions can be drawn:

1. Effect of Nano-particles volume fraction and size SiC_{mp}

   SiC_{np} predominantly acts as a reinforcement, bolstering the strength of the composite material. With an increase of SiC_{np} content, the beneficial interplay among particles induces an improvement in material ductility, which improves the overall GNDs, and the numerous 'dislocation sources' can coordinated to relieve the stress concentration at the SiC_{mp} tip. Smaller SiC_{np} size can better release stress concentration and increase the composite strength. Nevertheless, excessively large SiC_{np} sizes can weaken the strengthening effect and, in some cases, result in a decrease in material ductility.

2. Ratio of reinforcement particles with different sizes.

   These findings contribute to an enhanced understanding of the intricate interplay between particle size, volume fraction, and distribution in hybrid SiC_p/Al composites. Such insights are important for advancing the design and optimization of metal matrix composites with tailored mechanical properties. Consequently, the incorporation of SiC_{np} holds the potential to break the conventional trade-off barrier between strength and ductility. Effect of Nano-particles Size:

References

[1] G. Wang, G. Wang, Y.M. Zhang, Y.M. Wang, International journal of plasticity 164 (2023).

[2] Y.N. Zan, Y.T. Zhou, H. Zhao, Z.Y. Liu, Q.Z. Wang, D. Wang, W.G. Wang, B.L. Xiao, Z.Y. Ma, Composites Part B: Engineering 183 (2020) 107674.

[3] Y.N. Zan, Q. Zhang, Y.T. Zhou, Z.Y. Liu, Q.Z. Wang, D. Wang, B.L. Xiao, W.C. Ren, Z.Y. Ma, Composites Part B: Engineering 195 (2020) 108095.

[4] T. Han, E. Liu, J. Li, N. Zhao, C. He, Journal of Materials Science & Technology 46 (2020) 21-32.

[5] S.M. Schneider, V. Albert, N. Barbier, D. Barnoud, C. Bouteloup, C. Chambrier, P. Fayemendy, N. Flori, O. Goulet, D. Guimber, A. Jirka, F. Joly, D. Lescut, S. Neuville, M.-A. Piquet, F. Poullenot, D. Quilliot, D. Séguy, J. Stocco, R. Thibault, P. Déchelotte, Nutrition Clinique et Métabolisme 34(2) (2020) 105-107.

[6] K.K. Chawla, in: K.K. Chawla (Ed.), Composite Materials: Science and Engineering, Springer New York, New York, NY, 2012, pp. 197-248.

[7] M.J. Shen, X.J. Wang, M.F. Zhang, M.Y. Zheng, K. Wu, Composites Science and Technology 118 (2015) 85-93.

[8] M.Y. Zhou, L.B. Ren, L.L. Fan, Y.W.X. Zhang, T.H. Lu, G.F. Quan, M. Gupta, Journal of Alloys and Compounds 838 (2020) 155274.

[9] M.Y. Zhou, L.B. Ren, L.L. Fan, K.S. Tun, M. Gupta, Y.W.X. Zhang, T.H. Lu, G.F. Quan, Materials Science and Engineering: A 768 (2019) 138447.

[10] X. Zhang, C. Shi, E. Liu, F. He, L. Ma, Q. Li, J. Li, N. Zhao, C. He, Composites Part A: Applied Science and Manufacturing 103 (2017) 178-187.

[11] S. Ma, X. Zhang, T. Chen, X. Wang, Materials & Design 191 (2020) 108685.

[12] Q. Guo, W. Yao, W. Li, N. Gupta, Composite Structures 260 (2021) 113267.

[13] T. Kanit, S. Forest, I. Galliet, V. Mounoury, D. Jeulin, International Journal of Solids and Structures 40(13-14) (2003) 3647-3679.

[14] M.A. Eltaher, A. Wagih, Ceramics International 46(8, Part A) (2020) 10469-10480.

[15] L. Weng, T. Fan, M. Wen, Y. Shen, Composite Structures 209 (2019) 590-605.

[16] J.F. Zhang, H. Andrä, X.X. Zhang, Q.Z. Wang, B.L. Xiao, Z.Y. Ma, Composite Structures 226 (2019) 111281.
[17] B. Nayak, R.K. Sahu, Materials Research Express 6(11) (2019) 116593.
[18] Y. Peng, H. Zhao, J. Ye, M. Yuan, L. Tian, Z. Li, Z. Wang, J.a. Chen, Composite Structures 288 (2022) 115425.
[19] X. Zhou, Z.-f. Liu, F. Su, Y.-f. Fan, Transactions of Nonferrous Metals Society of China 31(3) (2021) 636-647.
[20] Z. Lin, Y. Su, C. Qiu, J. Yang, X. Chai, X. Liu, Q. Ouyang, D. Zhang, Scripta Materialia 224 (2023) 115135.
[21] Y. Huang, S. Qu, K.C. Hwang, M. Li, H. Gao, International Journal of Plasticity 20(4-5) (2004) 753-782.
[22] M. Ashby, The Philosophical Magazine: A Journal of Theoretical Experimental and Applied Physics 21(170) (1970) 399-424.
[23] H. Gao, Y. Huang, W.D. Nix, J.W. Hutchinson, Journal of the Mechanics and Physics of Solids 47(6) (1999) 1239-1263.
[24] H. Gao, Y. Huang, Scripta Materialia 48(2) (2003) 113-118.
[25] E. Hall, Proceedings of the Physical Society. Section B 64(9) (1951) 747.
[26] J.F. Zhao, X.C. Lu, F.P. Yuan, Q.H. Kan, S.X. Qu, G.Z. Kang, X. Zhang, International Journal of Plasticity 125 (2020) 314-330.
[27] J. Zhao, M. Zaiser, X. Lu, B. Zhang, C. Huang, G. Kang, X. Zhang, International Journal of Plasticity 145 (2021) 103063.
[28] Y. Wang, Y. Zhu, Z. Yu, J. Zhao, Y. Wei, Acta Materialia 241 (2022) 118395.
[29] J.J. Li, W.J. Lu, S.H. Chen, C.H. Liu, International Journal of Plasticity 126 (2020).
[30] J.J. Li, G.J. Weng, S.H. Chen, X.L. Wu, International Journal of Plasticity 88 (2017) 89-107.
[31] J.J. Li, A.K. Soh, International Journal of Plasticity 39 (2012) 88-102.
[32] J. Hutchinson, N. Fleck, Advances in applied mechanics 33 (1997) 295-361.
[33] J.F. Nye, Acta Metallurgica 1(2) (1953) 153-162.
[34] H. Zhou, C.X. Huang, X.C. Sha, L.R. Xiao, X.L. Ma, H.W. Hoppel, M. Goken, X.L. Wu, K. Ameyama, X.D. Han, Y.T. Zhu, Mater. Res. Lett. 7(9) (2019) 376-382.
[35] C.W. Sinclair, W.J. Poole, Y. Brechet, Scripta Materialia 55(8) (2006) 739-742.
[36] K. Cao, Z.-m. Yue, X.-d. Zhao, J. Qi, J. Gao, Journal of Materials Engineering and Performance 28(5) (2019) 3149-3156.
[37] H. Badreddine, K. Saanouni, A. Dogui, International Journal of Plasticity 26(11) (2010) 1541-1575.